$EuNi_2P_4$, the first magnetic unconventional clathrate prepared via mechanochemically assisted route

Igor V. Plokhikh[1], Nazir Khan[2], Alexander A. Tsirlin[2], Alexey N. Kuznetsov[3,4], Dmitri O. Charkin[3], Andrei V. Shevelkov[3] and Arno Pfitzner[1]

[1] Institute of Inorganic Chemistry, University of Regensburg, 93053 Regensburg, Germany

[2]Experimental Physics VI, Center for Correlations and Magnetism, Institute of Physics, University of Augsburg, 86135 Augsburg, Germany

[3]Lomonosov Moscow State University, 119991 Moscow, Russia

[4]Kurnakov Institute of General and Inorganic Chemistry RAS, 119991 Moscow, Russia

Abstract

For the first time, a magnetic unconventional clathrate $EuNi_2P_4$ has been prepared from the elements via a combined mechanochemical and solid-state route. Its crystal and electronic structure, magnetic and transport properties as well as lattice dynamics were elucidated. It crystallizes in the orthorhombic space group *Fddd* (Z = 8) with unit cell parameters a = 5.1852(1) Å, b = 9.4834(1) Å, and c = 18.9893(2) Å, V = 933.78(1) Å^3 at room temperature. Its crystal structure can be described as a covalent Ni – P framework forming a twisted Kelvin cell with Eu^{2+} guest cations occupying the voids of this framework, which is supported by chemical bonding analysis based on the Electron Localization Function topology. Eu^{2+} guests sit inside the oversized cages with a coordination number of 24 and exhibit strong rattling, which manifests in both thermodynamic properties and Raman spectra. The compound is metallic and exhibits a rather low thermal conductivity of ~4W/K/m at high temperature along with a positive Seebeck

coefficient. The magnetism of $EuNi_2P_4$ is predetermined by Eu^{2+} ($4f^7$) with dominant antiferromagnetic interactions. According to the magnetic susceptibility, heat capacity and resistivity measurements, $EuNi_2P_4$ undergoes three phase transitions at ~2.5 K, 6.1 K and 11.3 K in zero magnetic field.

Introduction

Intermetallic clathrates, the crystal chemical analogues of gas-hydrates [1], are known since long time and have been actively studied during the last few decades mostly due to their promising thermoelectric performance as well as other attractive physical properties ensuring their applications as photovoltaic, superconducting, and Li-ion batteries materials [2 – 5]. They can be generally described as tetrahedra of host-matrix atoms forming frameworks, which accommodate guest atoms with high coordination numbers. Frameworks of the classical anionic intermetallic clathrates are comprised by tetrel (Si, Ge and Sn) atoms that tend to maintain rather rigid ideal tetrahedral coordination. Classical clathrates crystallize in a limited number of structure types (or their superstructures) and prefer several typical space groups or their subgroups. Contrary to that, the frameworks of unconventional clathrates formed by pnictogen atoms are much more flexible and sustain more pronounced distortions of the classical clathrate polyhedra, thus giving rise to a more diverse crystallography [5 – 8]. Here, it is also worth mentioning that the presence of ions with high coordination numbers encapsulated into the frameworks leads to a wide range of so-called clathrate-like or clathrate-related compounds, as pointed out in a review [2] and exemplified by many compounds, including Eu containing examples [9].

An unconventional clathrate $SrNi_2P_4$ was recently reported [10] to be isostructural with the previously known $BaCu_2P_4$ [11] and has no analogs among gas hydrates, while $BaNi_2P_4$ adopts a different (and conventional) clathrate-VII structure type [12]. The crystal structure of $SrNi_2P_4$ and $BaCu_2P_4$ features 24-coordinated guest ions (Sr^{2+} and Ba^{2+}, respectively) occupying

24-vertex twisted Kelvin cells, thus filling the whole space. The Ba^{2+} ions in $BaNi_2P_4$ occupy a more symmetric truncated octahedron, *i.e.* this compound crystallizes in a distorted sodalite structure type. $BaNi_2P_4$ undergoes a tetragonal-to-orthorhombic distortion at ~373K [12] upon cooling or heating.

It is known that, unlike Ca and Ba, Eu commonly behaves as the closest analog of Sr [9, 13 – 15]. Therefore, we deduced the existence of a new compound, $EuNi_2P_4$ supposedly isomorphous to $SrNi_2P_4$. The radius of Eu^{2+} is comparable with that of Sr^{2+} [16], and the pnictide (phosphorus) environment ensures the stability of Eu^{2+} against Eu^{3+}. Among the classical intermetallic tetrel clathrates, rare examples of the Eu^{2+} magnetic ion introduced into the clathrate frameworks are known from the literature [17, 18]. Despite a substantial spatial separation in the $Eu_8Ga_{16}Ge_{30}$ structure, Eu^{2+} magnetic centers interact ferromagnetically, yielding a material exhibiting a pronounced magnetocaloric effect [19]. The example of $Eu_xBa_{8-x}Cu_{16}P_{30}$ shows that magnetic Eu^{2+} can be introduced into a framework of tetrel-free clathrates [20], but to the best of our knowledge, and contrary to the classical intermetallic clathrates, no pure-Eu^{2+} *magnetic* unconventional clathrates were reported till now.

Following this motivation, we attempted to prepare $EuNi_2P_4$ by a solid-state reaction in order to explore how the size, mass, electronic structure, and magnetism of the new guest ion would affect the behavior of the host matrix and the whole compound. First of all, Eu^{2+} is slightly smaller than Sr^{2+} (1.25 Å against 1.26 Å for the coordination number 8), which can cause a higher degree of mismatch between the guest ion and the framework that in turn renders this framework less stable. On the other hand, if it is indeed possible to incorporate Eu^{2+} into the title clathrate framework, a higher degree of mismatch should lead to more pronounced rattling. As rattling is believed to be responsible for the suppression of thermal conductivity (phonon-glass behavior), improved thermoelectric performance may be expected.

Magnetism of Eu^{2+} may also be interesting in this setting. On the one hand, the clathrate framework keeps the magnetic ions far from each other with nearest-neighbor distances over 5 Å. On the other hand, metallic nature of this framework facilitates long-range RKKY interactions that change sign depending on the Eu – Eu distance and may lead to complex magnetic behavior, which is indeed the case, as we show below. Last but not least, Eu^{2+}/Eu^{3+} valence fluctuations remain a possibility, as in EuPtP or $EuNi_2P_2$ [21, 22], and could further enrich the magnetic behavior. It has also been proposed that the mixing of 4*f* states of the lanthanide ion with itinerant states near the Fermi level can improve thermoelectric performance [20].

In the current paper, we report a mechanochemical synthesis as well as structural and thermodynamic study of the first magnetic unconventional clathrate, $EuNi_2P_4$, and compare it with the Sr analogue [10, 23].

Experiment

Synthesis and primary characterization. $EuNi_2P_4$ was prepared from the elements by a combined mechanochemical and solid-state route. All preparations were performed in an Ar-filled grove-box (MBraun, O_2 and H_2O less than 1ppm). Mixtures of metallic Ni (over 99.9%, purified from surface oxide in H_2 flow at 1073K), red phosphorus (over 99.5%, Chempur), and Eu (Novaelements, over 99.5% purity) were placed into silica tubes, flame-sealed under vacuum and annealed at 873K for 5 days. The as-prepared mixture was treated mechanochemically (600rpm, 3min milling + 5min cooling, 10 cycles) in a Pulverisette 7 ball-mill (Fritsch, Germany). The obtained powder was pressed into pellets 0.3 – 0.5 g each, flame-sealed in evacuated silica tubes and annealed at 1113K for 30 days. After that the sample was slowly cooled (0.1 K/min) to room temperature. Sample purity was checked using a STOE STADI P diffractometer (Mo-$K\alpha_1$ radiation, $\lambda = 0.70930$ Å, Ge (111) monochromator, Dectris Mythen 1K detector). Powdered samples were loaded in quartz capillaries of 0.3 mm diameter and spun

during the measurements at 293 K. The WinXPOW software package from STOE & Cie was used for data collection and processing [24]. A new compound isostructural with $SrNi_2P_4$ was found to be present in the sample as a majority phase. It is a black powder with metallic luster when compacted, stable in air over weeks. Elemental composition was confirmed using a Zeiss EVO MA 15 scanning electron microscope equipped with a Bruker Quantax EDX system with an X Flash Detector 630 M. Thermal behavior was studied *via* DTA technique utilizing a SETARAM TG-DTA 92 analyzer. The sample was loaded in silica capillaries and subjected to 2 heating and cooling cycles. It was found to irreversibly decompose at ~1120 K (see SI).

Temperature-dependent crystal structure determination. High-resolution synchrotron powder diffraction data were collected at the ID22 beamline of the European Synchrotron Radiation Facility (ESRF) (λ = 0.35414 Å) in the 10 – 273 K temperature range. For synchrotron measurements, samples were loaded into thin-walled borosilicate glass capillaries with an external diameter of 0.3 mm, and spun during the measurement. The diffracted intensity was collected by 8 scintillation detectors each preceded by a Si(111) analyzer crystal. The powder x-ray diffraction data were processed in the JANA2006 software. The crystal structure of $SrNi_2P_4$ was used as a starting model. The refinement was performed in a straight-forward manner using the standard mathematical apparatus for the Rietveld refinement implemented in JANA2006 [25]. Atomic displacement parameters of the light atoms (Ni and P) were refined in an isotropic approximation, while Eu was treated in an anisotropic approximation. The details of the powder diffraction experiment are collected in SI, a projection of the unit cell is depicted in **Figure 1**, the Rietveld refinement plot at 273 K is provided in **Figure 2**, and selected interatomic distances are given in **Table 1.**

Table 1. Selected interatomic distances (in Å) in the structure of $EuNi_2P_4$ at different temperatures.

Distance	10K	50K	100K	150K	250	273
Ni – P × 2	2.204(2)	2.206(2)	2.205(2)	2.205(2)	2.208(1)	2.209(2)

Ni – P× 2	2.212(2)	2.209(2)	2.211(2)	2.219(1)	2.219(1)	2.216(1)
Ni – Ni × 2	2.7008(1)	2.7013(1)	2.7019(1)	2.7024(1)	2.7083(1)	2.7094(1)
P – P	2.226(2)	2.225(2)	2.228(2)	2.222(2)	2.233(2)	2.232(2)
P – P × 2	2.226(2)	2.231(2)	2.228(2)	2.231(2)	2.221(2)	2.228(2)
Eu – Ni × 4	3.4447(7)	3.4443(7)	3.4450(7)	3.4482(6)	3.4502(6)	3.4491(6)
Eu – Ni × 4	3.6543(7)	3.6551(7)	3.6551(7)	3.6533(6)	3.6601(6)	3.6627(6)
Eu – P × 4	3.101(1)	3.098(1)	3.100(1)	3.101(1)	3.106(1)	3.107(1)
Eu – P × 4	3.106(1)	3.111(1)	3.110(1)	3.107(1)	3.115(1)	3.117(1)
Eu – P × 4	3.594(1)	3.595(1)	3.594(1)	3.592(1)	3.599(1)	3.602(1)
Eu – P × 4	3.842(1)	3.841(1)	3.842(1)	3.848(1)	3.848(2)	3.846(1)
Eu – Eu (the nearest)	5.17380(9)	5.17423(9)	5.17491(6)	5.17619(7)	5.18408(7)	5.18524(6)

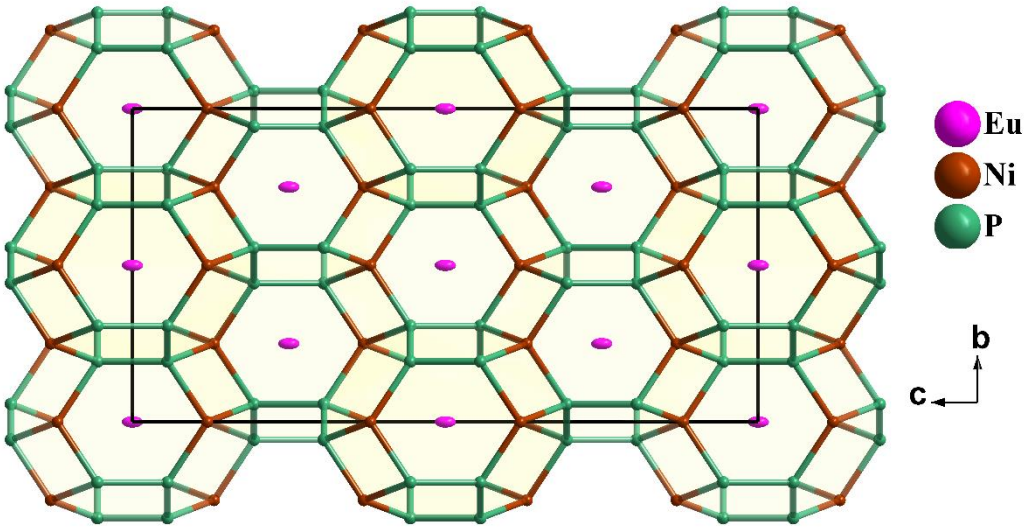

Figure 1. Projection of the $EuNi_2P_4$ unit cell along the *a*-direction in polyhedral representation. Cell edges are outlined in black. Thermal ellipsoids are drawn at 90 % probability level at 273 K.

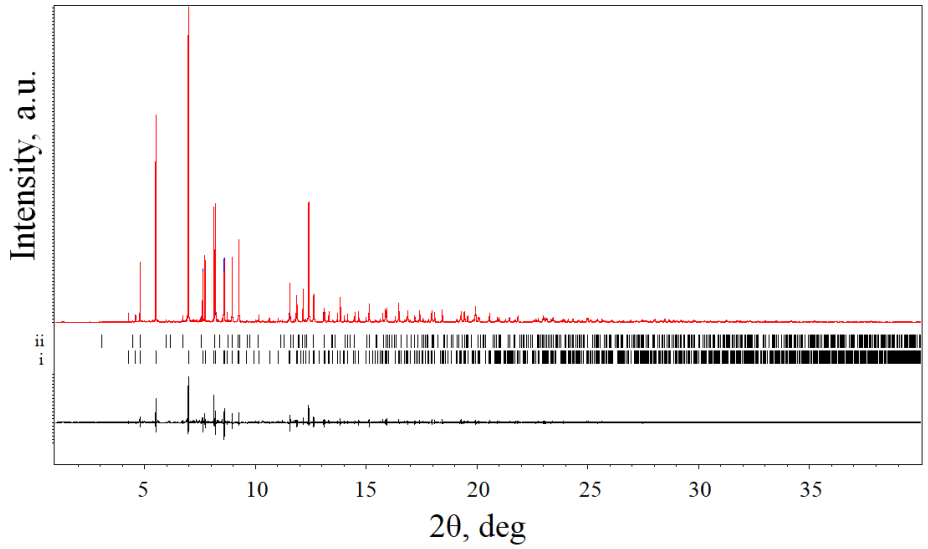

Figure 2. Synchrotron powder diffraction pattern of $EuNi_2P_4$ (phase i) at 273 K. A trace of $Eu_3(PO_4)_2$ impurity (phase ii), amounting ~1.6 weight %, is included into the refinement. The calculated line is shown in blue, experimental points are red, difference curve and positions of the reflections are black.

Magnetic, heat capacity, and thermoelectric properties measurements. The temperature and field dependence of the magnetization was measured using a Quantum Design SQUID-VSM magnetometer (MPMS 3). The specific heat was measured in a Quantum Design Physical Properties Measurement System (QD-PPMS 14 T) using the relaxation method. Temperature dependence of zero-field thermal conductivity, Seebeck coefficient, and electrical resistivity were measured using the Thermal Transport Option (TTO) of the QD-PPMS. The sample was cut in a brick-like shape with the dimensions of 8.4 mm × 2.25 × 2.5 mm^2. The four-probe configuration was made by mounting four gold-plated copper leads to the sample using silver-filled epoxy. Data were collected in the continuous measurement mode by slowly sweeping the temperature from 300 K down to 2 K at the rate of 0.25 K/min. The Seebeck coefficient was found to be below 1 μV/K, which cannot be precisely measured using TTO setup.

Raman spectroscopy. Raman spectra were measured on a home-made Raman spectrometer equipped with a HeNe laser providing 35 mW at 632 nm and a CCD camera attached to a grating spectrograph with 350 mm focal length and 1800/mm grating for the signal detection. Find a detailed description of the setup in SI.

Electronic structure calculations and vibration spectra simulations. Density Functional Theory (DFT) based calculations were performed using the pseudopotential projector augmented wave method (PAW) as implemented in the Vienna *ab initio* Simulation Package (VASP) [26, 27]. A Monckhorst-Pack *k*-point mesh of 10 × 10 × 8 was employed, and the energy cutoff was set at 500 *eV* [28]. The PBE exchange-correlation functional of the GGA-type was used in the PAW-based calculations [29]. In order to account for the Eu^{2+} *f*-orbitals, a special potential for

Eu^{2+}, supplied with the VASP package, was used, which puts localized *f*-orbitals into the core. The convergence of the total energy with respect to the *k*-point sets was checked. Atomic charges in the direct-space analysis were calculated according to Bader's QTAIM approach [30, 31]. The electron localization function (ELF) was calculated by the internal VASP routine according to [32]. A Raman spectrum for $EuNi_2P_4$ was simulated based on the Density Functional Perturbation Theory (also known as Linear Response Theory), with Raman frequencies obtained from VASP phonon calculations using the script from Fonari & Stauffer [33]

Results and discussion

Synthesis. According to literature [10, 23], samples of $SrNi_2P_4$ can be easily prepared from the elements by several subsequent annealing steps at 1123 K. Contrary to that, when a stoichiometric mixture of Eu, Ni, and P is subjected to the same synthetic procedure, the yield of the target crystalline phase of $EuNi_2P_4$ does not exceed 80 %, with all samples containing sizeable amounts of $EuNi_2P_2$ and phosphorus as by-products. Reducing the temperature to 973 K does not improve the sample quality, heating above 1123 K leads to an irreversible decomposition observed by DTA measurements, whereas below 873 K reaction kinetics becomes too slow. Therefore, other methods (growth from salt melt, high-pressure synthesis, and mechanochemical activation) were tried. As only the mechanochemical route was successful, we will discuss only this procedure. The described synthetic procedure was checked to be scalable up to at least 3 g. Here, we also would like to mention that despite the existence of numerous compounds in the ternary Eu – Ni – P system ($EuNi_2P_2$ [22], $Eu_8Ni_{18}P_{11}$ [34], $Eu_9Ni_{26}P_{12}$ [35], $Eu_2Ni_7P_4$ [36], $EuNi_5P_3$ [37], $Eu_2Ni_{12}P_5$ [38], $Eu_2Ni_{12}P_7$ [39] and two modifications of $EuNi_{10}P_6$ [40]) and some recent synthetic attempts [41], our new compound, $EuNi_2P_4$, expands the P-rich region of the Eu-Ni-P system.

Crystal structure and its temperature dependence. A projection of the $EuNi_2P_4$ crystal structure is provided in **Figure 1.** It can be described similarly to $SrNi_2P_4$ as a Ni – P framework

with the Eu^{2+} cations placed into its voids. Each Ni atom is surrounded by 4 phosphorus atoms at a distance of 2.20 – 2.22 Å, forming distorted tetrahedra. The NiP_4 tetrahedra share common edges forming infinite NiP_2 chains. These chains are linked by P – P bridges and form 24-vertex polyhedra that fill the whole space. In general, the details of the crystal structures of $SrNi_2P_4$ and $EuNi_2P_4$, including distances and angles, are very similar if not identical.

On decreasing the temperature the unit cell volume decreases, as it is shown in **Figure 3**, and so do the unit cell parameters as well as most of the interatomic distances (in SI). When comparing the cell parameters of $EuNi_2P_4$ (a = 5.175 Å, b = 9.456 Å, c = 18.975 Å, V = 928.5 $Å^3$ at 100 K) and $SrNi_2P_4$ (a = 5.193 Å, b = 9.560 Å, c = 18.958 Å, V = 941.1 $Å^3$ at 90 K), one can notice that the a, b parameters and cell volume follow the trend expected from ionic radii, while the c parameter behaves in an opposite way. Also, below 150 K both $EuNi_2P_4$ and $SrNi_2P_4$ [23] exhibit almost zero thermal expansion along the c-axis. Despite Eu being the heaviest atom in the structure, its room-temperature atomic displacements parameter (ADP) is substantially higher than for Ni and P. It also exhibits a pronounced anisotropy: the U_{33} is almost twice as high as U_{11}. Such an anomaly is attributed to the fact that the distances between the center of the cage (the ideal position of an Eu atom) and the atoms comprising the cage exceed 3 Å, while the cage itself is elongated along the c-direction, *i.e.* the Eu^{2+} cation follows its shape.

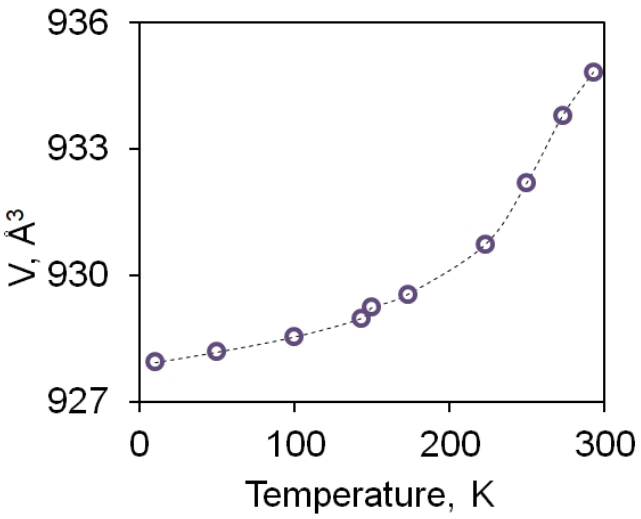

Figure 3. Temperature dependence of the unit cell volume of $EuNi_2P_4$. The graph combines both synchrotron and laboratory diffractometer data.

As the temperature decreases, the atomic displacement parameters also decrease (**Figure 4**). All presented ADP lines tend to low, though not zero, values, pointing to the fact that, some minor static disorder still persists [42]. ADPs on Eu atoms decrease much faster with temperature than on Ni and P atoms. At 100 K they are already comparable, while at 10 K the ADPs of Eu are twice smaller than those of Ni and P (in SI). Nevertheless, the anisotropy of Eu ADPs' still persists. For the data in the temperature region of 50 K – RT the temperature increments of ADP are $3.99 \cdot 10^{-5}$, $3.02 \cdot 10^{-5}$ and $9.24 \cdot 10^{-5}$ $Å^2/K$ for U_{11}, U_{22} and U_{33} of Eu respectively, and $1.15 \cdot 10^{-5}$, $1.99 \cdot 10^{-5}$ $Å^2/K$ for Ni and P respectively. Note that Ni and P were refined with isotropic ADPs. Deviations from the linearity of the atomic displacements parameters for the 10 K data (in SI) is already significant.

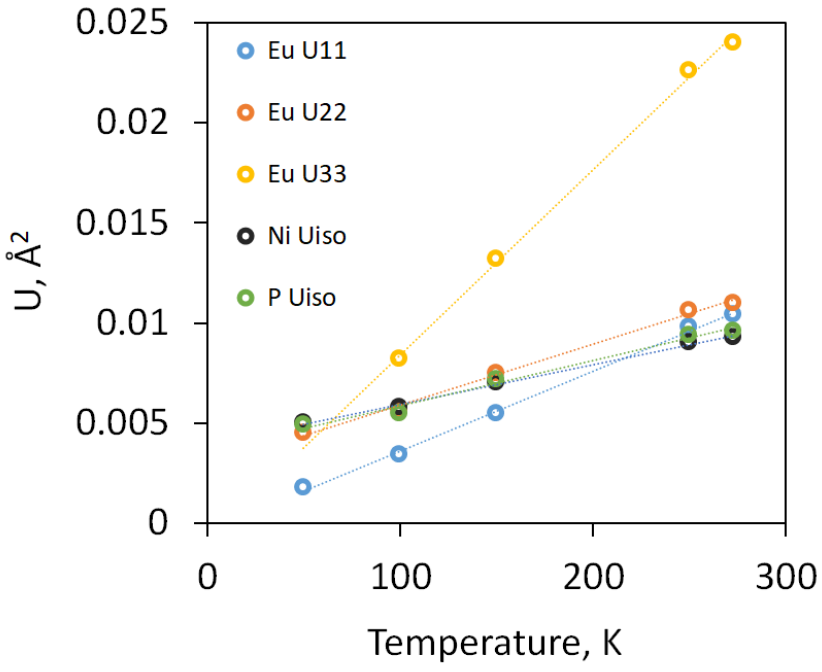

Figure 4. Temperature dependence of the isotropic ADPs of Ni and P, and of the anisotropic ADP tensor components (U_{11}, U_{22} and U_{33}) for Eu.

Assuming that Ni and P obey the Debye model, their slope of the *U(T)* functions can be expressed as:

$\frac{3h^2}{4\pi M\theta_D^2 k_B}$, where θ_D is a characteristic Debye temperature and *M* is the atomic mass [42].

The slope of the *U*(*T*) function for Eu yields the characteristic Einstein temperature θ_E of the quasi-free guest atom according to the expression:

$\frac{h^2}{8\pi^2 m\theta_E k_B}\coth(\frac{\theta_E}{2\pi})$, where *m* is the atomic mass of the oscillator (Eu^{2+}) [42].

Thus, the averaged Debye temperature from the data for Ni and P can be estimated as 475 K; the Einstein temperature from the U_{33} of Eu is 104 K (equivalent to 0.015 *eV* or 72 cm^{-1}) and the averaged Einstein temperature from U_{11} and U_{22} of Eu is 170 K.

Electronic Structure.

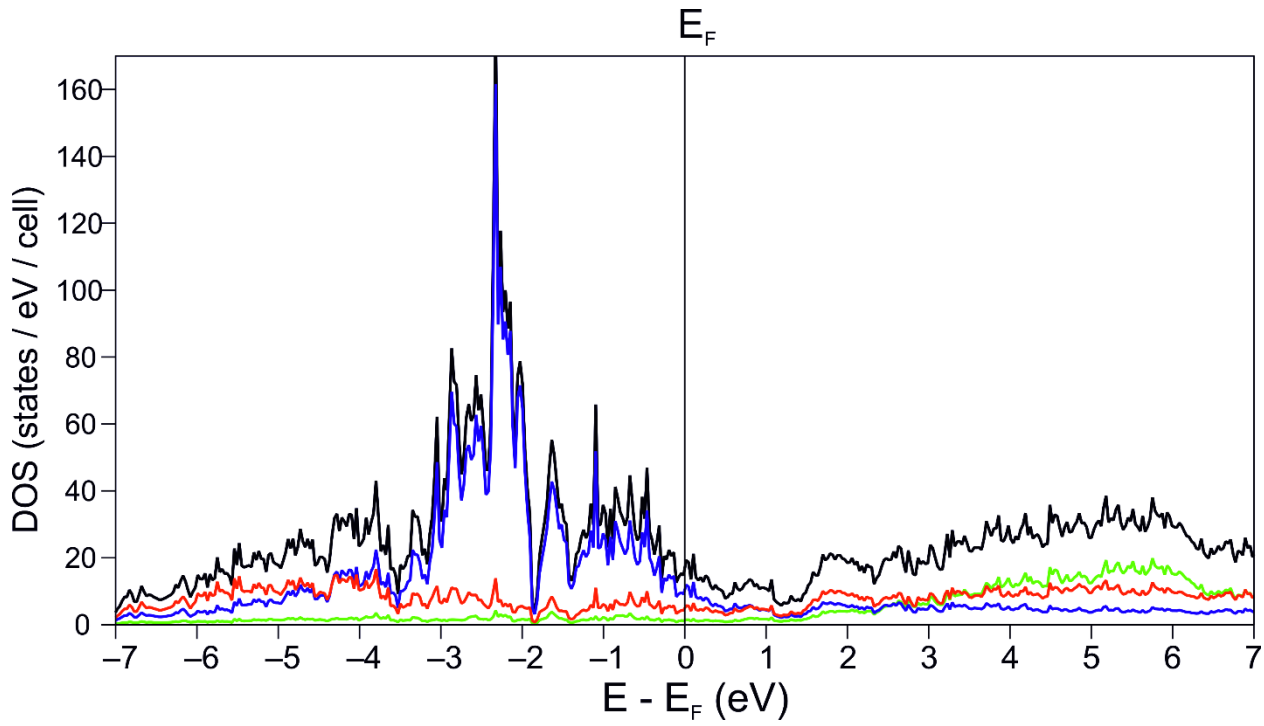

Figure 5. Total (TDOS) and projected (PDOS) density of states near the Fermi level for $EuNi_2P_4$: green – Eu PDOS, blue – Ni PDOS, P – red PDOS.

Calculated densities of states near the Fermi level for $EuNi_2P_4$ are shown in **Figure 5**. Non-zero density of states at the Fermi level indicates the metallic nature of this compound. Main contributions under the Fermi level are provided by the 3*d* states of Ni atoms, with 3*p* states of P also contributing at the Fermi level, albeit to a significantly lesser extent. Eu *d*-states mostly contribute to the region above the Fermi level, which is consistent with its supposedly cationic Eu^{2+} character (see magnetic data below). In general, the DOS for $EuNi_2P_4$ is very similar to that of $SrNi_2P_4$ [10], complete with the pseudo-gap at ca. -1.9 eV. The mixing of the Ni and P states at the Fermi level may possibly imply a certain degree of covalency in the Ni-P bonds. This is confirmed by the calculated Bader atomic charges, which are: +1.4 (Eu), +0.1 (Ni), -0.4 (P). Low charges on the Ni and P atoms also indicate covalent bonding contributions between the nickel and phosphorus atoms.

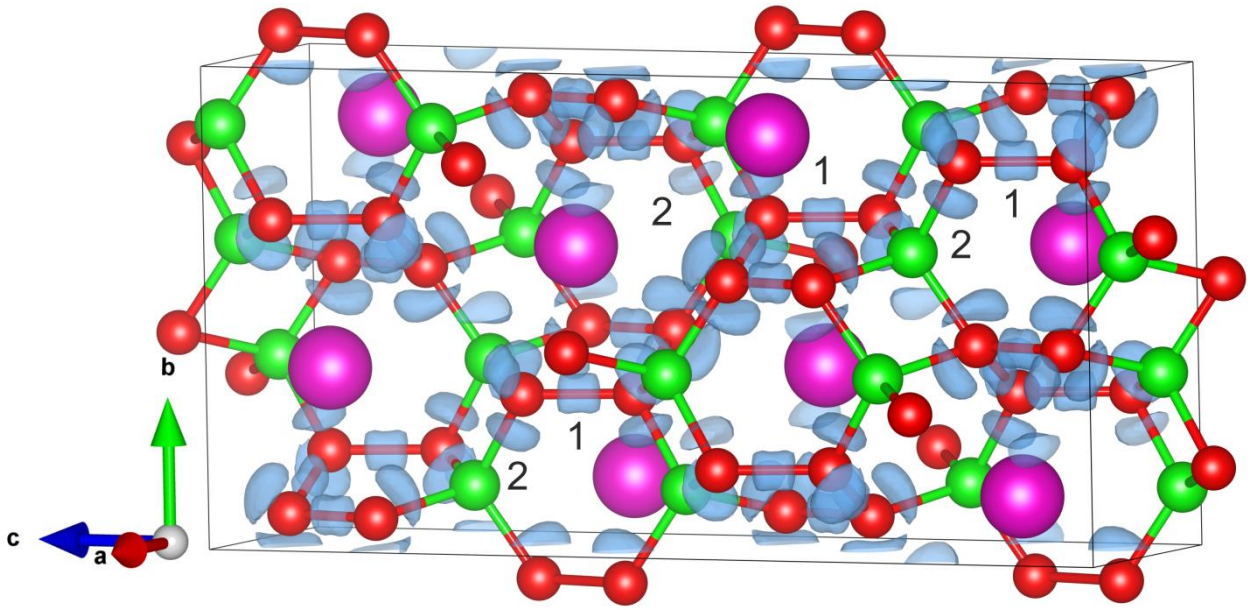

Figure 6. ELF isosurface (η = 0.80) for $EuNi_2P_4$: 1 – P – P bonds, 2 – Ni – P bonds. Ni atoms are shown in green, Eu in pink, P in red, ELF isosurface in blue.

To gain more insight into the bonding pattern in $EuNi_2P_4$, we performed a topological analysis of the Electron Localization Function (ELF), which allows to observe atomic shells, lone pairs, or bonds in direct space. For $EuNi_2P_4$ we clearly see two distinct kinds of the non-atomic ELF attractors presented in **Figure 6**: localization domains 1 and 2 corresponding to the pairwise P – P and Ni – P interactions. The P - P bond domains are completely symmetrical and apparently correspond to classical two-center non-polar covalent bonds. The Ni - P bond attractors are shifted towards phosphorus atoms, which means that the Ni - P bond has a degree of polarity (which agrees well with calculated atomic charges). The Ni - P bond localization domains also show asymmetry and are slightly shifted from the lines connecting Ni and P atoms towards the Eu cations in the voids. We have investigated the structuring of the phosphorus valence shell more closely, in order to see if additional type of attractor might be present that could influence the shape of the Ni-P bond domains, but found no extra ELF maxima (see SI). Thus, we can interpret the bonding in $EuNi_2P_4$ as europium cations embedded into the essentially covalent network of the Ni – P and P – P bonds.

Magnetic measurements. Temperature dependence of magnetic susceptibility in different fields as well as the Curie-Weiss fit are presented in **Figure 7**. Above 15 K, the sample behaves as a Curie –Weiss paramagnet with the derived magnetic moment of 7.93 μ_B per formula unit, consistent with divalent Eu, assuming that Ni and P are non-magnetic (the expected value for pure Eu^{2+} is 7.94 μ_B). The Curie-Weiss temperature θ_{CW} = – 5.72 K is negative, which points to the overall antiferromagnetic interactions in $EuNi_2P_4$.

A magnetic susceptibility curve taken at 0.005 T shows several anomalies below 15 K. From the dχ/dT plot (provided in SI) we infer the critical temperatures of 2.5 K, 4.1 K, 6.1 K, 7.8 K and 11.3 K. The 4.1 K and 7.8 K anomalies are already almost invisible in 0.025 T field and completely blurred in 0.1 T (**Figure 7**); they were not confirmed from heat capacity and resistivity measurements. Therefore, they are either extrinsic and caused by an impurity like $Eu_3(PO_4)_2$ that orders antiferromagnetically below 5 K [43], or arise from valence fluctuations

(Eu^{2+}/Eu^{3+}) similar to $EuNi_2P_2$ at low temperature [22]. The low-temperature behavior was further elucidated by combination of heat capacity measurements, temperature-dependent magnetic susceptibility and field-dependent magnetization data.

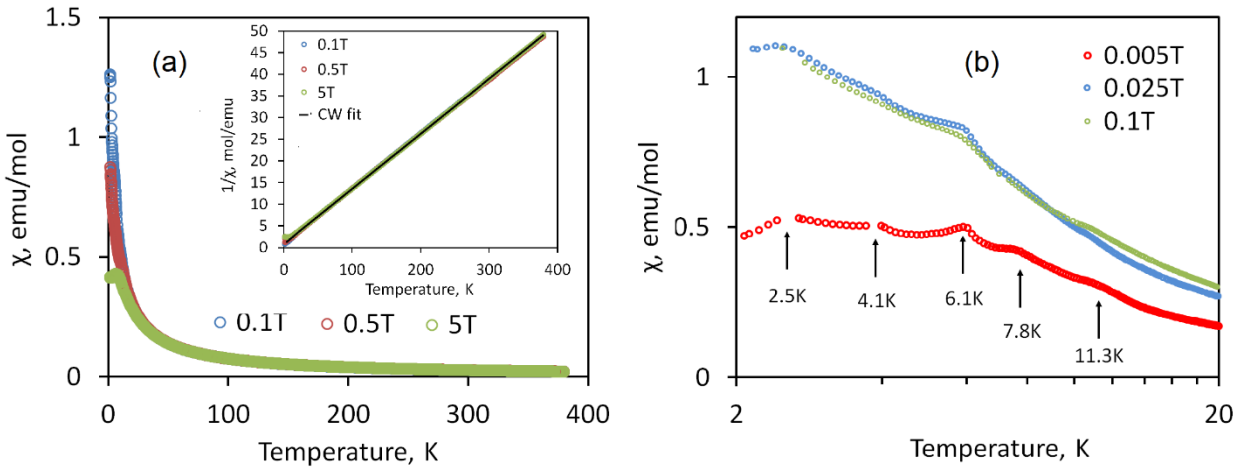

Figure 7. (a) Temperature dependence of the magnetic susceptibility ($\chi = M/H$) taken in the fields of 0.1 T, 0.5 T and 5 T, and the Curie-Weiss fit shown as insert. (b) Low-temperature part of the magnetic susceptibility curve measured in the 0.005 T, 0.025 T and 0.1 T applied fields. The positions of anomalies are identified from the first derivative (SI).

Magnetization curves taken at different temperatures are shown in **Figure 8.** Magnetization at 1.9 K increases with increasing field with one distinct inflection point at 5.2 T and several broad anomalies in lower fields. The positions of those anomalies were located from the d*M*/d*H vs T* curve (provided in SI) and labeled on **Figure 8.** The 5.2 T anomaly does not exhibit hysteretic behavior, while the positions of the low-field anomalies (especially the one at ~1 T) substantially change upon switching the direction of the field. The strongly non-linear shape of the 1.9 K magnetization curve is consistent with the effects observed in the magnetic susceptibility data. Several anomalies are also observed in the 5 K magnetization curve, while the magnetization curve at 9 K and above is close to linear.

The curve measured at 1.9 K does not reach saturation even at 7 T; the highest magnetic moment is 5.4 μ_B/f.u., *i.e.* 20 % less than the expected value of 7 μ_B for pure Eu^{2+}. This fact further confirms sizable antiferromagnetic interactions between the Eu^{2+} moments.

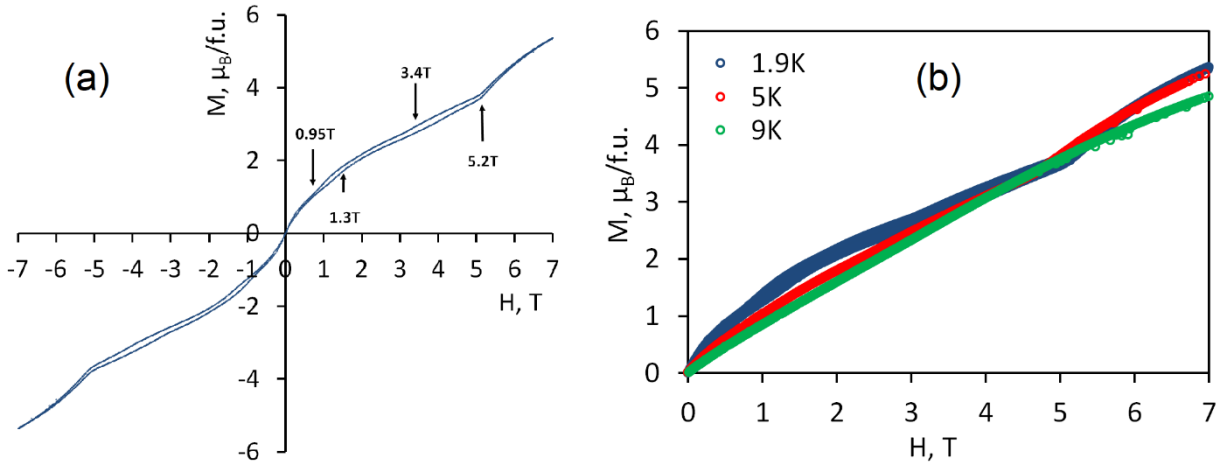

Figure 8. (a) Magnetization curve (magnetic moment *vs* applied field) taken at 1.9K. Three transitions at ~ 1 T, ~3.4 T, and 5.2 T are visible. The first two transitions exhibit a hysteresis. (b) Magnetization curves taken at 1.9 K, 5 K, and 9 K.

Heat capacity measurements. The heat capacity of $EuNi_2P_4$ also shows several anomalies (**Figure 9**). The large anomaly at 11.3 K signals a second-order magnetic transitions, while another pronounced anomaly at 2.5 K and a small anomaly around 6 K are first-order in nature. At low-temperatures, between 2 and 6 K, a broad hump, similar to that in $SrNi_2P_4$, is observed. Otherwise, the heat capacity curve below 15 K is smooth, suggesting that two other anomalies observed in the low-field susceptibility at 4.1 K and 7.8 K are likely extrinsic.

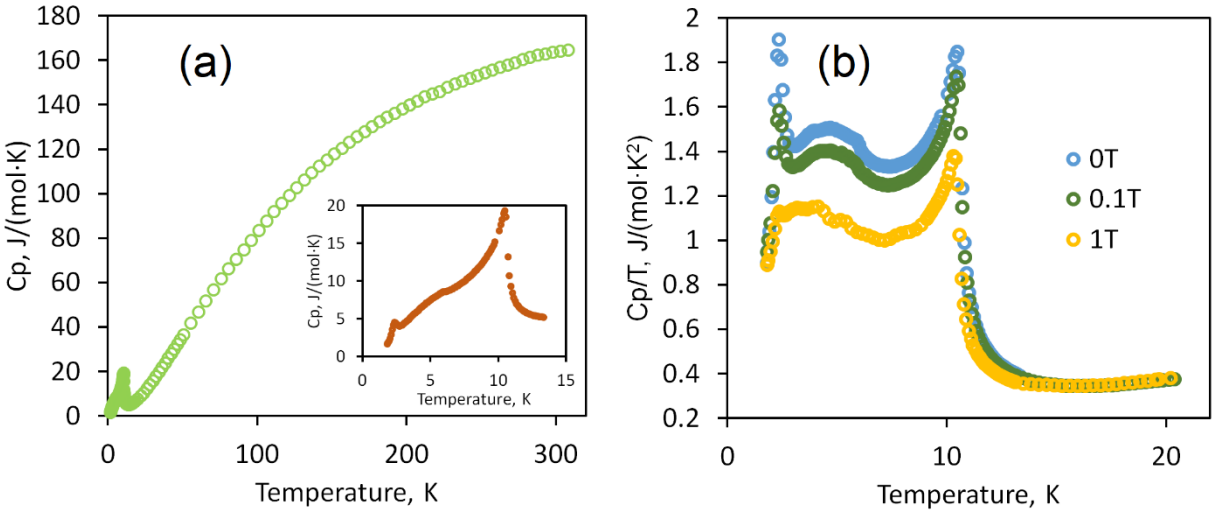

Figure 9. (a) Heat capacity measured from room temperature down to 2K with the low-temperature part shown as insert. (b) Low-temperature part of the heat capacity measured in different fields plotted as C_p/T *vs* T.

Above 15 K, the heat capacity curve is smooth, confirming the absence of phase transitions in this region. The heat capacity curve does not reach saturation at room temperature, while approaching the Dulong–Petit limit $C_p = N{\times}3R$ = 7 3·8.31 = 174.5 J/(mol·K), where N is the number of atoms per formula unit. The C_p/T^3 *vs* T^2 plot (in SI) intended to disclose a possible contribution from the Einstein modes caused by rattling is dominated by the magnetic transition at 11.3 K. Within the 15 K – 250 K temperature region, it is possible to fit the data with the following equation, similar to $SrNi_2P_4$ [23]:

$$C_V \approx C_P = a_D C_D\left(\frac{\theta_D}{T}\right) + a_{E1} C_E\left(\frac{\theta_{E1}}{T}\right) + a_{E2} C_E\left(\frac{\theta_{E2}}{T}\right)$$

We can argue that, similarly to $SrNi_2P_4$, the second Einstein term is due to a substantial anisotropy of the Eu^{2+} vibrations, which is evident from **Figure 4.** Indeed, our attempts to fit the heat capacity curve with the pure Debye model or with the Debye model supplied by a single Einstein mode were unsuccessful (see SI). In contrast, the model with two Einstein modes leads to a perfect fit up to 250 K, and the characteristic temperatures are θ_D = 521 K, θ_{E1} = 73 K, θ_{E2} = 159 K.

Resistivity and thermoelectric properties. Temperature dependence of the resistivity (inverse electrical conductivity) and thermal conductivity measured on a pressed and sintered polycrystalline sample with ~85% density are shown in **Figure 10**. Whereas a contribution of grain boundaries cannot be excluded, we were nevertheless able to extract basic trends in transport properties. On increasing the temperature, the resistivity increases from 0.5 μΩ·m at 25 K to 3.5 μΩ·m at 300 K, confirming the metallic behavior of $EuNi_2P_4$. Linear temperature dependence of the resistivity indicates electron-phonon interaction as the main scattering mechanism. The Seebeck coefficient is within the range of 0.6 – 0.9 μV/K at 10 – 300 K. The small but positive value of the Seebeck coefficient pinpoints the *p*-type conductivity in $EuNi_2P_4$. Above ~10K, thermal conductivity rapidly increases reaching ~4W/K·m at 100K. The electronic component of the thermal conductivity was calculated according to the Wiedemann–Franz law [10] and plotted together with the total thermal conductivity in **Figure 10**.

The low-temperature resistivity presented in **Figure 11** shows anomalies at 2.7 K and 11.3 K, which are consistent with the magnetic susceptibility and heat capacity data and confirm the intrinsic nature of the magnetic transitions.

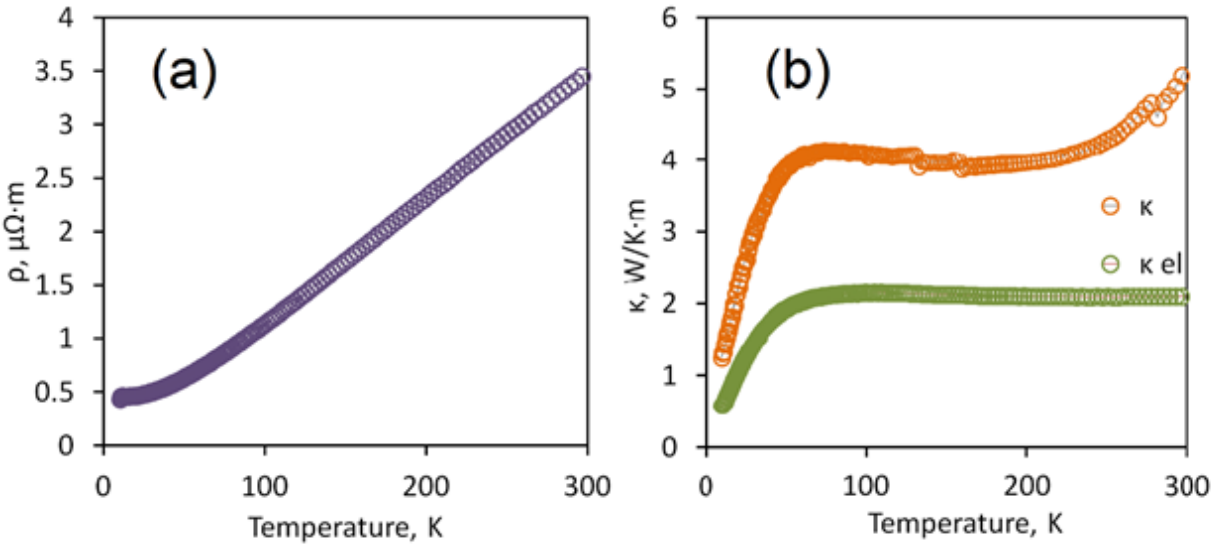

Figure 10. Temperature dependence of the resistivity (a), and thermal conductivity (b) in the 10 – 300K temperature range.

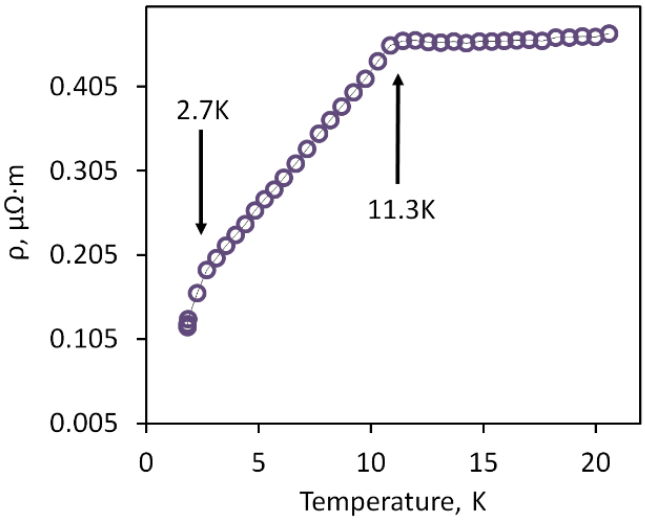

Figure 11. Low-temperature part of the electrical resistivity curve for $EuNi_2P_4$.

Raman spectroscopy data. Raman spectroscopy helps observing rattling modes in clathrates [44, 45]. The Raman spectrum of $EuNi_2P_4$ shown in **Figure 12** reveals a very strong vibration mode at 59 cm^{-1} that corresponds to a temperature of 85 K. The high-wavenumber region (also above 190 cm^{-1}) is featureless, which may signal that other modes are too weak to be distinguished over the background, given the strong absorption is caused by the metallic nature of the material.

The high Debye temperature of ~500 K suggests that the observed Raman mode does not belong to phonons of the host matrix. On the other hand, the mode frequency agrees very well with the characteristic values calculated from the slope of U_{33} of Eu (104 K) and with the low-energy contribution to the heat capacity (73 K). However, such a simplified consideration does not explain the absence of the second mode at a slightly higher energy, which would be expected from the anisotropic movements of Eu^{2+} inside the cage.

In order to get further insight into the Raman spectra, we calculated Raman-active vibrational modes in $EuNi_2P_4$. The obtained positions along with their relative intensities are the following: 65 cm^{-1} (100%), 71 cm^{-1} (1.5%), 92 cm^{-1} (0.6%), 94 cm^{-1} (0.4%), 367 cm^{-1} (4%), 401 cm^{-1} (7%), 409 cm^{-1} (3%). First of all, the only intense mode is at 65cm^{-1}, which is in a very

good agreement with the observed one at 59cm^{-1}. The second point is that Γ-point phonons can be split into two parts well separated in energy. The low-energy modes below 100 cm^{-1} are responsible for the Eu^{2+} rattling, whereas the high-energy modes are caused by vibrations of the host matrix. The presence of more than two calculated low-energy modes suggests that even the anisotropic harmonic model for the description of ADPs of the rattler is not fully adequate.

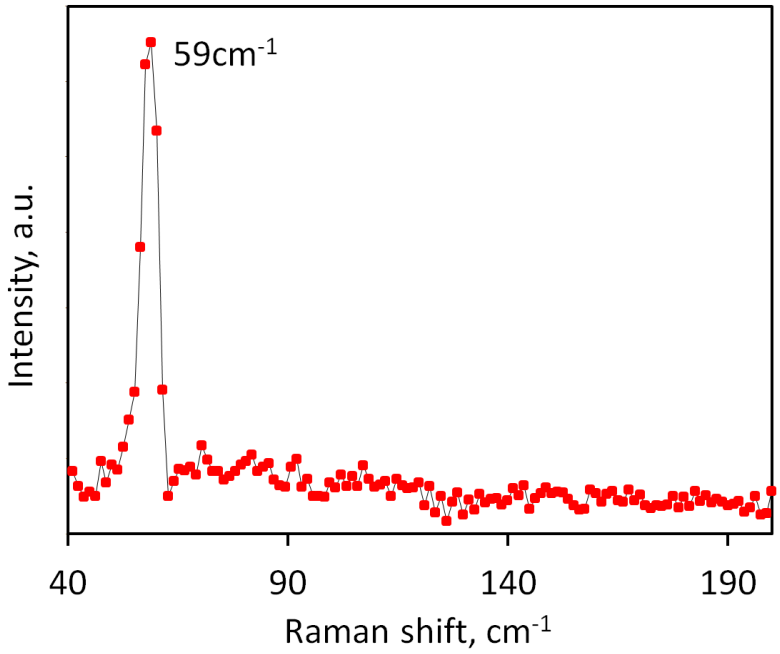

Figure 12. A room-temperature Raman spectrum of $EuNi_2P_4$ features a single intense mode at 59 cm^{-1}.

General overview and structure-properties relations. $EuNi_2P_4$ is the first representative of magnetic unconventional clathrates. Compared to $SrNi_2P_4$, the synthesis of the Eu analogue proved to be more difficult, given the size difference between Sr^{2+} and Eu^{2+}. Still the effect of the size mismatch between Eu^{2+} and the Ni – P framework in $EuNi_2P_4$ is somehow mitigated by re-assembling of the twisted Kelvin cell into a more symmetric ("less twisted") cage, as suggested by the trend in the unit cell dimensions of $SrNi_2P_4$ and $EuNi_2P_4$.

Unlike the majority of solids, clathrates cannot be described by the Debye lattice model. It is often assumed that phonon spectra of clathrates can be separated into two nearly

independent parts. One of them corresponds to vibrations of the host matrix that occur at higher energies and can be described by the Debye model. As guest cations are located in the oversized cages, their movements are independent from the host matrix and can be described by pseudo-localized Einstein modes. The estimated Debye temperatures of $SrNi_2P_4$ and $EuNi_2P_4$ are comparable and lie around 500 K, as the frameworks of the two compounds are almost identical. The characteristic Einstein temperatures extracted from the heat capacity data for Eu^{2+} in $EuNi_2P_4$ (73K) and Sr^{2+} in $SrNi_2P_4$ (reported 71 K [23]) are also comparable. This close similarity can be explained by two counteracting effects, because Eu^{2+} has a higher mass but a slightly smaller radius compared to Sr^{2+}.

According to the transport properties data, $EuNi_2P_4$ exhibits a behavior similar to $SrNi_2P_4$, though its resistivity is slightly lower, while thermal conductivity is slightly higher. It is interesting that the thermal conductivity of $SrNi_2P_4$ almost exclusively arises from the electronic term, while in $EuNi_2P_4$ lattice and electronic contributions are comparable in magnitude. This could be explained by the presence of 4*f* electronic states near the Fermi level, as it has been outlined elsewhere [20]. However, the extracted magnetic moment of Eu suggests the absence of valence fluctuations and the full localization of 4*f* electrons on the Eu atoms.

Although Eu^{2+} magnetic cations are well separated in the crystal structure with the shortest Eu – Eu distance of 5.17 Å, sizable magnetic interactions occur. Our data reveal at least three phase transitions at ~2.5 K, ~6.1 K and ~11.3 K. According to the structural data, there are no structural transformations in $EuNi_2P_4$ down to 10K. The transition at 11.3 K is of second order and probably due to an antiferromagnetic ordering in the Eu sublattice, the transition at 6.1K is also of magnetic nature, while the one at ~2.5K is a first-order transition with a magnetic component.

The antiferromagnetic nature of $EuNi_2P_4$ is underpinned by the fact that the magnetization curve taken at 1.9 K shows a complex non-linear shape and does not reach

saturation in a 7 T field. The negative Curie-Weiss temperature (θ_{CW} ~ – 5.7 K) reflects predominant antiferromagnetic interactions too, but its absolute value is twice smaller than the Neel temperature T_N = 11.3 K. The complex low-temperature behavior observed in $EuNi_2P_4$ is rather unusual for magnetic clathrates. Magnetic interactions between the Eu^{2+} magnetic ions are mediated by conduction electrons through the RKKY mechanism and can be either ferro- or antiferromagnetic depending on the Eu – Eu distance. $EuNi_2P_4$ features several nearest-neighbor Eu – Eu distances that fall in the 5.17 – 5.42 Å range, and may thus combine ferro- and antiferromagnetic interactions, leading to a complex magnetic behavior.

The low-temperature phase diagram of $EuNi_2P_4$ (**Figure 13**) reveals three distinct phases that transform into each other as a function of temperature and field. The outer phase boundary is typical for antiferromagnets, whereas the other phase boundaries may reflect additional magnetic or structural order. Our preliminary neutron diffraction measurements confirm three low-temperature magnetically ordered phases; the derived magnetic structures will be communicated later.

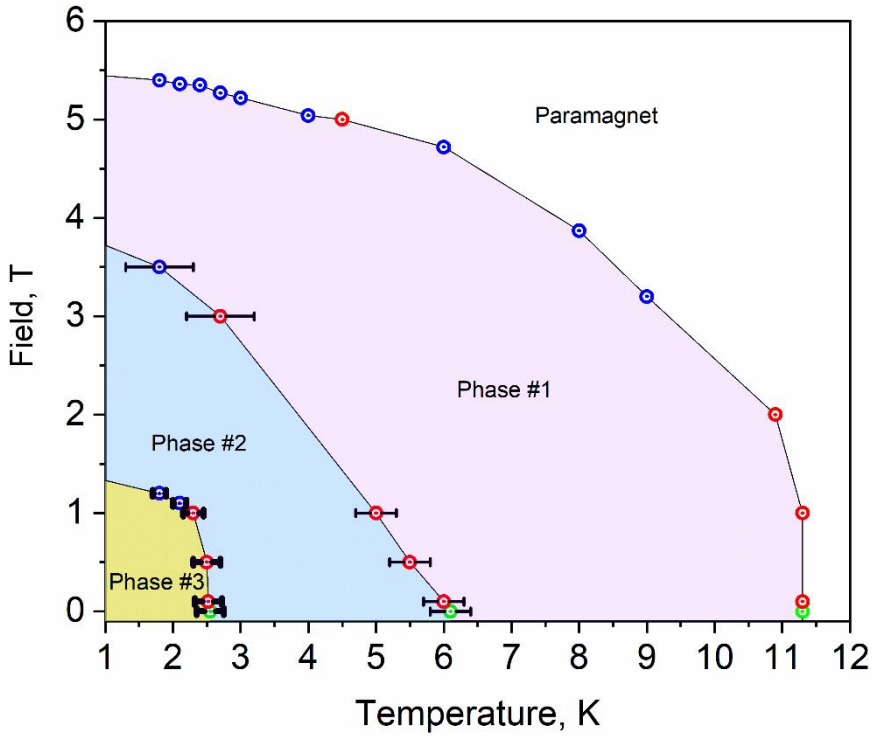

Figure 13. Field *vs* temperature phase diagram of $EuNi_2P_4$. Blue points are taken from isothermal sections (magnetization *vs.* field), red – from constant field sections (magnetization *vs.* temperature), green – averaged zero-field data. The error bars are due to the hysteresis of first-order transitions.

Conclusions

$EuNi_2P_4$ is a new magnetic compound that extends the family of unconventional clathrates and provides the first example of a purely magnetic guest atom. This compound can be prepared by a combined mechanochemical and solid-state reaction. In its crystal structure, Eu^{2+} cations are encapsulated into 24-coordinated metallic twisted Kelvin cells formed by the Ni and P atoms. Pronounced rattling of the Eu^{2+} cation inside the oversized cage results in a strong Einstein contribution to the heat capacity, and is also evident from the Raman scattering and temperature-dependent diffraction data. Despite the large spatial separation between the Eu^{2+} magnetic centers, predominantly antiferromagnetic interactions occur. $EuNi_2P_4$ reveals complex magnetism with three phase transitions at 2.5 K, 6.1 K and 11.3 K in zero field. Metallic nature of $EuNi_2P_4$ leads to rather poor thermoelectric performance.

Acknowledgements

We thank Prof. Alkwin Slenczka for the Raman measurements. The work was supported by DAAD *via* a doctoral scholarship for Igor V. Plokhikh. The work in Augsburg was supported by the German Federal Ministry for Education and Research through the Sofija Kovalevskaya Award of the Alexander von Humboldt Foundation (AAT). Research in Moscow has been supported by the Russian Science Foundation, grant # 16-12-00004; ANK and DOC acknowledge the support from Russian Foundation for Basic Research (Grant No. 18-03-01201 a). The calculations were carried out using the equipment of the shared research facilities of the HPC computing resources at Lomonosov Moscow State University.

References

[1] Jeffrey, G.A. In: Hydrate Inclusion Compounds; Atwood, J.L., Davies, J.E., McNicol, D.D., Eds.; Academic Press: London, **1984**.

[2] Shevelkov, A.V.; Kovnir K. Zintl Clathrates. In: Fässler T. (ed) Zintl Phases. Structure and Bonding, vol 139. Springer, Berlin, Heidelberg, **2010**.

[3] Kovnir, K.A.; Shevelkov, A.V. Semiconducting clathrates: synthesis, structure and properties. *Russ. Chem. Rev.* **2004**, *73*, 923 – 938.

[4] The Physics and Chemistry of Inorganic Clathrates; Nolas, G. S., Ed.; Springer: New York, **2014.**

[5] Dolyniuk, J.-A.; Owens-Baird, B.; Wang, J.; Zaikina, J.V.; Kovnir K. Clathrate thermoelectrics. *Materials Science and Engineering: R: Reports*, **2016**, *108*, 1 – 46

[6] Wang, J.; Dolyniuk J.-A.; Kovnir, K. Unconventional clathrates with transition metal–phosphorus frameworks, *Accounts of Chemical Research*, **2017**, *51*, 31 – 39.

[7] Dolyniuk, J.; Whitfield, P. S.; Lee, K.; Lebedev, O. I.; Kovnir, K. Controlling superstructural ordering in the clathrate-I $Ba_8M_{16}P_{30}$ (*M* = Cu, Zn) through the formation of metal–metal bonds. *Chem. Sci.* **2017**, *8*, 3650 – 3659

[8] Dolyniuk, J.-A.; Zaikina, J.V.. Kaseman D.C.; Sen S.; Kovnir, K. Breaking the tetra-coordinated framework rule: new clathrate $Ba_8M_{24}P_{28+\delta}$ (M=Cu/Zn). *Angew. Chem.* **2017**, *56*, 2418 – 2422.

[9] Charkin, D.O.; Demchyna, R.; Prots, Yu.; Borrmann, H.; Burkhardt, U.; Schwarz, U.; Schnelle, W.; Plokhikh, I.V.; Kazakov, S.M.; Abakumov, A.M.; Batuk, D.; Verchenko, V.Yu.; Tsirlin, A.A.; Curfs, C.; Grin, Yu.; Shevelkov, A.V. Two new arsenides, $Eu_7Cu_{44}As_{23}$ and $Sr_7Cu_{44}As_{23}$, with a new filled variety of the $BaHg_{11}$ structure. *Inorg. Chem.* **2017**, *53*, 11173 – 11184.

[10] Dolyniuk, J.-A.; Wang, J.; Lee, K.; Kovnir, K. Twisted kelvin cells and truncated octahedral cages in the crystal structures of unconventional clathrates, AM_2P_4 (*A* = Sr, Ba; M = Cu, Ni). *Chem. Mater.* **2015**, *27*, 4476 – 4484.

[11] Dünner, J.; Mewis, A. $BaCu_2P_4$-ein neues ternäres Polyphosphid. *Journal of the Less Common Metals*. **1990**, *167*, 127 – 134.

[12] Keimes, V.; Johrendt, D.; Mewis, A.$BaNi_2P_4$: Dimorphie durch Peierls-Verzerrung? Z. *Anorg. Allg. Chem.* **1995**, *621*, 925 – 930.

[13] Suen, N.-T.; Huang, L.; Meyers, J.J.; Bobev, S. An unusual triple-decker variant of the tetragonal $BaAl_4$-structure type: synthesis, structural characterization, and chemical bonding of $Sr_3Cd_8Ge_4$ and $Eu_3Cd_8Ge_4$. *Inorg. Chem.* **2018**, *57*, 833 – 842.

[14] Zhang, R.; Pan, M.-Y.; Zhu, M.; Tao, X.-T.; Xia, S.-Q. Experimental and theoretical studies on the crystal structure of ternary copper arsenides $A_2Cu_3As_3$ (A = Sr, Eu). *Eur. J. Inorg. Chem.* **2016**, *23*, 3774 – 3780.

[15] Charkin, D.O.; Urmanov, A.V.; Kazakov, S.M.; Batuk, D.; Abakumov, A.M.; Knoner, S.; Gati, E.; Wolf, B.; Lang, M.; Shevelkov, A.V.; Van Tendeloo, G.; Antipov, E.V. Synthesis, crystal structure, transport, and magnetic properties of novel ternary copper phosphides, $A_2Cu_6P_5$ (A = Sr, Eu) and $EuCu_4P_3$. *Inorg. Chem.* **2012**, *51*, 8948 – 8955.

[16] Shannon, R. D. Revised effective ionic radii and systematic studies of interatomic distances in halides and chalcogenides. *ActaCryst. A* **1976**, 32, 751 – 767.

[17] Mudryk, Y.; Rogl, P.; Paul, C.; Berger, S.; Bauer, E.; Hilscher, G.; Godart, C.; Noël, H.; Saccone, A.; Ferro. R. Crystal chemistry and thermoelectric properties of clathrates with rare-earth substitution. *Physica B*, **2003**, *328*, 44 – 48.

[18] Sales, B. C.; Chakoumakos, B. C.; Jin, R.; Thompson, J. R.; Mandrus, D. Structural, magnetic, thermal, and transport properties of $X_8Ga_{16}Ge_{30}$ (*X* = Eu, Sr, Ba) single crystals. *Phys. Rev. B* **2011**, *63*, 245113.

[19] Phan, M. H.; Woods, G. T.; Chaturvedi, A.; Stefanoski, S.; Nolas, G. S.; Srikanth, H. Long-range ferromagnetism and giant magnetocaloric effect in type VIII $Eu_8Ga_{16}Ge_{30}$ clathrates. *Appl. Phys. Lett*. **2008**, *93*, 252505.

[20] Kovnir, K.; Stockert, U.; Budnyk, S.; Prots, Y.; Baitinger, M.; Paschen, S.; Shevelkov, A.V.; Grin, Y. Introducing a magnetic guest to a tetrel-free clathrate: Synthesis, structure, and properties of $Eu_xBa_{8-x}Cu_{16}P_{30}$ ($0 \leq x \leq 1.5$). *Inorg. Chem.* **2011**, *50*, 10387 – 10396.

[21] Johrendt, D.; Felser, C.; Huhnt, C.; Michels, G.; Schäfer, W.; Mewis A.Tuning the valence in ternary Eu-pnictides: the series $EuPd_{1-x}Ag_xP$ and $EuPd_{1-x}Au_xAs$. *J. All. Com.* **1997**, *246*, 21 – 26

[22] Perscheid, B.; Sampathkumaran, E.V.; Kaindl, G. Temperature and pressure dependence of the mean valence of Eu in $EuNi_2P_2$. *J. Magn. Magn. Mater.* **1985**, *47 – 48*, 410 – 412

[23] Novikov, V.; Pilipenko, K.; Matovnikov, A.; Mitroshenkov, N.; Plokhikh, I.; Tyablikov, A.; Shevelkov, A. Structure-related thermal properties of type-VII clathrates $SrNi_2P_4$ and $BaNi_2P_4$ at low temperature. *Phys. Status Solidi*, **2018**, *255*, 1800067.

[24] STOE WinXPOW, Version 3.10, STOE &Cie GmbH, Darmstadt **2016**.

[25] Petricek, V.; Dusek, M.; Palatinus, L. Crystallographic computing system JANA2006: general features. *Z. Kristallogr.* **2014**, *229*, 345.

[26] Kresse, G.; Furthmüller, J. Vienna Ab initio simulation package (VASP), v.5.3, http://www.vasp.at/

[27] Kresse, G.; Joubert, D. From ultrasoft pseudopotentials to the projector augmented-wave method. *Phys. Rev. B* **1999**, *59*, 1758 – 1775.

[28] Monckhorst, H. J.; Pack, J. D. Special points for Brillouin-zone integrations. *Phys. Rev. B.* **1976**, *13*, 5188.

[29] Perdew, J.P.; Burke, K.; Ernzerhof, M. Generalized gradient approximation made simple. *Phys. Rev. Lett.* **1996**, *77*, 3865 – 3868.

[30] Bader, R.F.W. Atoms in Molecules: a Quantum Theory, Oxford University Press, Oxford, **1990**.

[31] Yu, M.; Trinkle, D.R. Accurate and efficient algorithm for Bader charge integration, *J. Chem. Phys.* **2011**, *134*, 064111.

[32] Silvi, B.; Savin, A. Classification of chemical bonds based on topological analysis of electron localization functions. *Nature.* **1994**, *371*, 683.

[33] A. Fonari, S. Stauffer. Vasp_raman.py, Python program to evaluate off-resonance Raman activity using VASP code, 2013. https://github.com/raman-sc/VASP/

[34] Chykhrij, S.I.; Babizhets'ky; V.S., Oryshchyn S.V.; Kuz'ma Yu.B.; Aksel'rud, L.G. Crystal structure of $Tb_{16}Ni_{36}P_{22}$ and isotypic lanthanoid nickel phosphides. *J. Alloys Compd.* **1997**, *259*, 186 – 190.

[35] Babizhets'ky, V.S.; Chykhrij, S.I.; Oryshchyn, S.V.; Kuz'ma, Yu.B. Preparation of the new phosphides $Ln_9Ni_{26}P_{12}$ (Ln= Ce, Pr, Nd, Eu) and their crystal structure. *Russ. J. Inorg. Chem.* **1992**, *37*, 1372 – 1374.

[36] Babizhets'ky, V.S.; Chykhrij, S.I.; Oryshchyn, S.V.; Kuz'ma, Yu.B. Synthesis and structure of some new phosphides of rare-earth metals and nickel. *Ukr. Khim. Zh. (Ukr. Ed.)*. **1993**, *59*, 240 – 242.

[37] Badding, J.V.; Stacy, A.M. Synthesis and crystal structure of a new europium nickel phosphide phase, $EuNi_5P_3$. *J. Solid State Chem.* **1987**, *67*, 354 – 358.

[38] Kuz'ma, Yu.B.; Babizhet'sky, V.S.; Chykhrij, S.I.; Oryshchyn, S.V.; Pecharsky V.K. Preparation and crystal structure of the $La_2Ni_{12}P_5$ and isotypic ternary lanthanoid-nickel phosphides. *Z. Anorg. Allg. Chem.* **1993**, *619*, 587 – 592.

[39] Jeitschko, W.; Jaberg, B. Neue Verbindungen mit $Zr_2Fe_{12}P_7$-Struktur und Verfeinerung der Kristallstrukturen von $Er_2Co_{12}P_7$ und $Er_2Ni_{12}P_7$. Z. *Anorg. Allg. Chem.* **1980**, *467*, 95 – 104.

[40] Keimes, V.; Hellmann, A.; Mewis, A.; C. Huhnt, C.; Schütte, N. $SrNi_{10}P_6$, $EuNi_{10}P_6$ und $BaCo_{10}As_6$: Phasenumwandlungen und Kristallstrukturen. *Z. Anorg. Allg. Chem.* **2000**, *626*, 1653 – 1659.

[41] Dolyniuk, J.-A.; Mark, J.; Lee, S.; Tran, N.; Kovnir K. Synthesis and characterization of K and Eu binary phosphides. *Materials.* **2019**, *12*, 251.

[42] Sales, B.C.; Mandrus, D.G.; Chakoumakos, B.C. Use of atomic displacement parameters in thermoelectric materials research *Semiconduct. Semimet.* **2001**, *70*, 1-36

[43] Mayer, I.; Fischbein, E.; Cohen, S. Apatites of divalent europium *J. Solid State Chem.* **1975**, *14*, 307 – 312.

[44] Nolas G.S.; Kendziora, C. A. Raman scattering study of Ge and Sn compounds with type-I clathrate hydrate crystal structure. *Phys. Rev. B* **2000**, *62*, 7157.

[45] Takasu, Y.; Hasegawa, T.; Ogita, N.; Udagawa, M.; Avila, M.A.; Suekuni, K.; Ishii, I.; Suzuki, T.; Takabatake. T. Dynamical properties of guest ions in the type-I clathrate compounds $X_8Ga_{16}Ge_{30}$ (X = Eu, Sr, Ba) investigated by Raman scattering. *Phys. Rev. B* **2006**, *74*, 174303.